



## Regular Article

Flash spark plasma sintering of  $\text{HfB}_2$  ceramics without pre-sinteringJi Zou <sup>a,\*</sup>, Salvatore Grasso <sup>b,c</sup>, Lei-Feng Liu <sup>a</sup>, Hai-Bin Ma <sup>d</sup>, Mike Reece <sup>a</sup>, Jon Binner <sup>a</sup><sup>a</sup> School of Metallurgy and Materials, University of Birmingham, B15 2TT Birmingham, UK<sup>b</sup> School of Engineering and Material Science, Queen Mary University of London, London, UK<sup>c</sup> Key Laboratory of Advanced Technologies of Materials, Ministry of Education, School of Materials Science and Engineering, Southwest Jiaotong University, Chengdu 610031, China<sup>d</sup> Chinese Nuclear Power Technology Research Institute, 518026 Shenzhen, China

## ARTICLE INFO

## Article history:

Received 24 June 2018

Received in revised form 15 July 2018

Accepted 19 July 2018

Available online xxxx

## Keywords:

Borides

Flash spark plasma sintering

Sintering

Microstructure

## ABSTRACT

Strong  $\text{HfB}_2$  powder green bodies with compressive strengths exceeding 20 MPa have been produced by incorporating 1 wt% of glassy carbon derived from a pyrolyzed phenolic resin binder. Starting from the green body after debinding in argon, non-textured  $\text{HfB}_2$  ceramics (diameter ~ 20 mm and height ~ 4 mm) with a relative density of 95.1% were achieved using flash spark plasma sintering (FSPS) with a discharge time of 20 s, peak power of 19 kW and applied pressure of ~16 MPa. The lack of a need for a pre-sintering step resulted in energy savings compared to the densification of  $\text{HfB}_2$  ceramics by FSPS.

© 2018 Acta Materialia Inc. Published by Elsevier Ltd. All rights reserved.

Sintering is an essential step in the production of almost all ceramics; however, conventionally it is both time and energy intensive. A significant saving in both factors has been recently realised via “flash sintering (FS)” [1]. This process involves application of an electric field across a ceramic green body to promote Joule heating. Under constant voltage mode, a flash event (a sharp increase in the temperature of the sample) can be triggered when the furnace temperature exceeds a threshold value. This allows ceramics to be densified in a matter of seconds [2, 3]. A thermal runaway-based model can predict the heat balance; the flash occurs when the Joule heating significantly exceeds the heat dissipation to the nearby environment [2–6].

Previous investigations, however, have recognised that an inhomogeneous temperature distribution exists within samples during flash sintering [7]. Such inhomogeneity is reduced when the green body has a dog-bone shape and this special geometry is also chosen to maintain a uniform field across the sample, as well as a volumetric power dissipation [7, 8]. To reduce the need for such a specific geometry requirement, with a cross section limited to a few square millimetres and sample weight to typically below 1 g, a modified configuration for FS has been implemented using a spark plasma sintering (SPS) furnace [9–13]. Various ceramics, including SiC [11],  $\text{ZrB}_2$  [9],  $\text{ZrO}_2$  [12] and  $\text{B}_4\text{C}$  [13], with diameters up to 60 mm have been consolidated by the flash spark plasma sintering (FSPS) in less than a minute.

A green body for a typical FSPS process has to be strong enough to withstand the thermal stresses resulting from the rapid heating, whilst the compressive strength also has to exceed the contact force of the SPS

apparatus. The latter is required to ensure good electrical contact and so avoid electrical arcing/overheating at the contacts of the punch-die-ram assembly. Pre-sintering of the pellets at a relatively low temperature and pressure has been commonly adopted to obtain a suitably strong body for FSPS; the relative density of the ceramic body after pre-sintering is normally between 45% and 63.6% [9, 12]. For example,  $\text{ZrB}_2$  and yttria-stabilized zirconia green bodies were pre-sintered by SPS at 1600 °C/16 MPa/20 min [9] and 750 °C/30 MPa/1 min [12], respectively. This need clearly reduces the potential advantages of FSPS in terms of overall time and energy savings.

In the present work, the green strength of the ceramics was increased by the incorporation of 1 wt% of glassy carbon into the ceramic matrix.  $\text{HfB}_2$ , a well-known ceramic that is hard-to-densify [14–16], e.g. hot pressing at 2200 °C/30 MPa for 60 min only yielded 85.8% of the theoretical density [14], was used to demonstrate the potential of this method during FSPS.

$\text{HfB}_2$  ( $D_{50}$  = 3.7  $\mu\text{m}$ , C: 0.1 wt%, O: 0.2 wt%, Treibacher, Althofen, Austria) and 2 wt%  $\text{B}_4\text{C}$  ( $D_{50}$  = 0.5  $\mu\text{m}$ , H.C. Starck, grade BF-12, Goslar, Germany) powders were ball mixed together in ethanol for 24 h. In some batches, 2.43 wt% phenolic resin (PR, Hexion Inc., Rotterdam, The Netherlands) was added into the slurry before mixing [14, 15]. The slurry was subsequently dried at 40 °C for 0.5 h to remove all the solvent; simultaneous magnetic stirring was employed in order to avoid any possible sedimentation during drying. The resulting dried powder cake was crushed into fine powders, which were then die pressed at 200 MPa into pellets with a diameter of 20 mm and height of 5 mm using a steel mould preheated to 40 °C to soften the phenolic resin. The green body was pyrolyzed at 600 °C for 2 h in argon using a heating rate of 1 °C/min to convert the phenolic resin into carbon. The

\* Corresponding author.

E-mail addresses: [j.zou@bham.ac.uk](mailto:j.zou@bham.ac.uk), [zouji1983@aliyun.com](mailto:zouji1983@aliyun.com) (J. Zou).

compressive strength of the green bodies before and after pyrolysis at 600 °C (denoted as P-RT and P-600) were measured using 5 mm  $\Phi$   $\times$  10 mm height cylindrical samples under a load displacement rate of 0.5 mm/min.

FSPS runs were conducted in a commercial SPS furnace (FCT HPD 25; FCT Systeme GmbH, Rauenstein, Germany) under vacuum. The general details are given elsewhere [11]. The as-pyrolyzed, pressed HfB<sub>2</sub> green bodies were wrapped with a layer of 4 mm thick graphite felt to avoid the effect of radiative heat loss as much as possible and to minimize the temperature difference across the sample during heating. Each sample was placed between the two graphite punches and a pre-load of 5 kN was applied in order to achieve good electrical contact. After some initial trials, a maximum power of between 10 and 20 kW, depending on the discharging time and the relative pre-set power of the SPS, was chosen. Two discharging times, 20 and 35 s, were finally adopted whilst the corresponding relative power was set at 100% and 80%, respectively. During FSPS the temperature was measured using two pyrometers, one was located at the top of the furnace and focused on the graphite punch at a distance of 4 mm from the sample, whilst the second was located on the side of the furnace and focused on the graphite felt covering the sample.

The density of the resultant samples was measured using the Archimedes' method in water and converted to a relative density using a theoretical value calculated using the rule of mixtures for appropriate volume proportions of HfB<sub>2</sub>, B<sub>4</sub>C and C. Scanning electron microscopy, SEM (JEOL 7000, Tokyo, Japan), was used to observe the fracture surfaces of the green bodies as well as polished surfaces of the sintered bodies. A dual-beam FIB/FEG-SEM equipped with an EBSD detector was employed to look for the evidence of crystallographic texture in the flash sintered samples. Orientation maps were obtained from the surfaces perpendicular to the loading direction and the step size for the EBSD scans was 0.2  $\mu$ m. A misorientation angle larger than 5° was used to determine the mean grain size and its distribution in the sintered ceramics. A 200 kV JEOL TEM (2100F) equipped with electron energy loss spectrometry (EELS, GIF 963, Gatan, USA) was used to detect the features and locations of any as-pyrolyzed carbon in the HfB<sub>2</sub> matrix.

Without phenolic resin additions, HfB<sub>2</sub> – 2 wt% B<sub>4</sub>C powders could not be pressed into crack-free pellets. According to the manufacturer, the phenolic resin used in this work had a pyrolytic carbon (PyC) yield of 41 wt% after pyrolysis. Using this, the calculated composition in the green body after pyrolysis was HfB<sub>2</sub> – 2 wt% B<sub>4</sub>C – 1 wt% C. Average compressive strengths of  $9.6 \pm 0.3$  and  $20.2 \pm 0.7$  MPa were measured for P-RT and P-600, respectively. Since 20 mm diameter samples were used for FSPS, the maximum compressive load that the P-600 samples could take was  $\sim 10$  kN. This value was greater than the minimum load (5 kN) applied by the SPS equipment during its initial loading.

The behaviours of P-RT and P-600 (the relative density of both was  $\sim 55\%$ ) under uniaxial compression are compared in Fig. 1a. P-RT shows classic ductile behaviour, which explains the better shaping behaviour of the powder mixture when PR was present. In contrast, no apparent plastic deformation prior to failure was observed in P-600 indicating that these samples fractured in a brittle manner with an enhanced compressive strength value.

As may be observed within the backscattered SEM image of P-RT in Fig. 1b, there were a number of grains with slightly darker contrast that were well distributed within the HfB<sub>2</sub> matrix. The average HfB<sub>2</sub> primary particle size from Fig. 1b is 1.25  $\mu$ m, significantly smaller than the D<sub>50</sub> value (3.7  $\mu$ m) provided by the manufacturer, indicating agglomeration existed in the raw powders. Considering that the mean atomic numbers of both PR and B<sub>4</sub>C are much smaller than for HfB<sub>2</sub>, these darker grains must be either PR or B<sub>4</sub>C. The EDS analysis results shown in Fig. 1d & e revealed that point A is PR whilst point B is B<sub>4</sub>C. The oxygen and carbon signals in PR, Fig. 1d, are much stronger than those in B<sub>4</sub>C, Fig. 1e. After pyrolysis, flakes with thickness  $< 100$  nm were observed occasionally on the fracture surface of P-600; highlighted by arrows in Fig. 1c. It seems that these nanostructures were derived from the pyrolysed PR. Previous work has shown that the densification of HfB<sub>2</sub> by hot pressing starts above 1650 °C [14], therefore, the strength improvement in P-600 compared to P-RT cannot be ascribed to partial sintering since the heat treatment only occurred at 600 °C. As a result, the different behaviour under compression between P-RT and P-600 must be due to the conversion from PR to PyC. To illuminate this further, the bonding characteristics between the PyC and HfB<sub>2</sub> particles were further investigated using

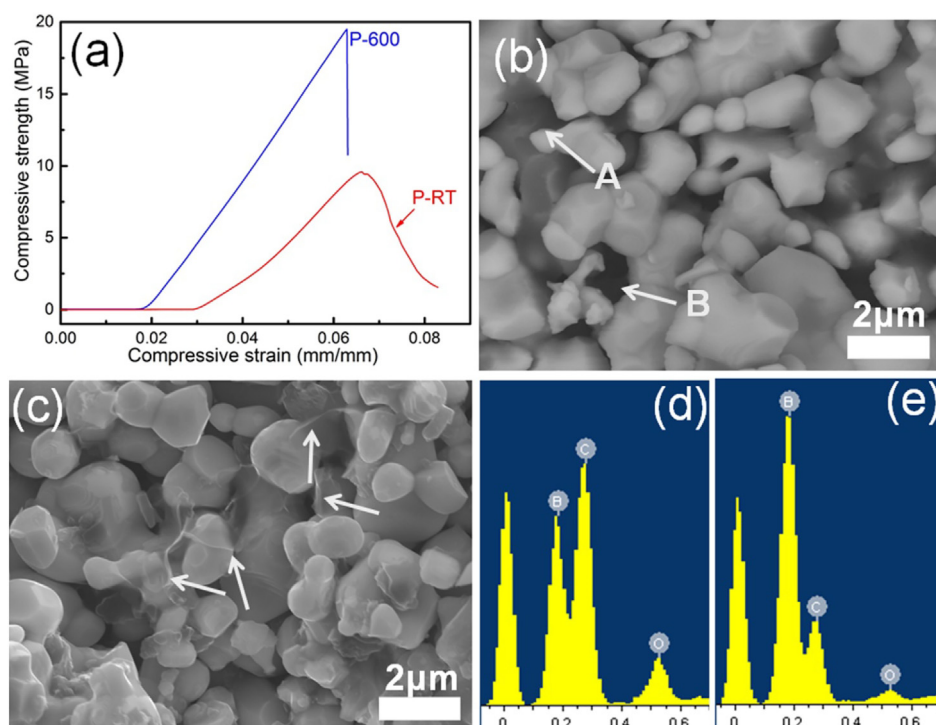
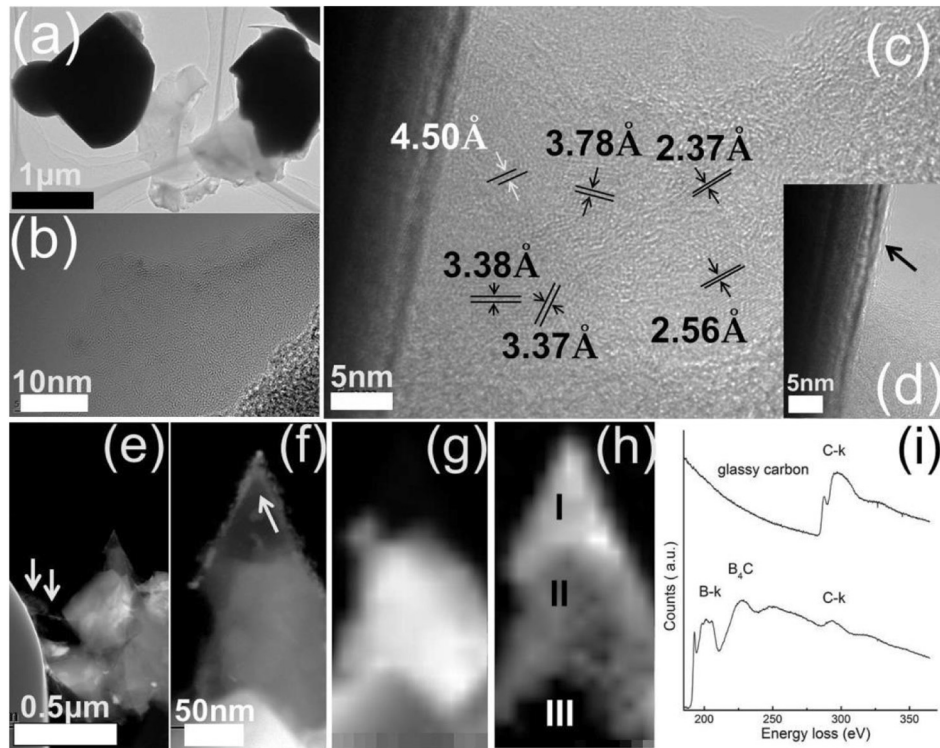


Fig. 1. a. Compressive strain-stress curve for P-RT and P-600. b. & c. fracture surfaces of P-RT and P-600, respectively. d. & e. EDS analysis of point A and B highlighted in Fig. 1b.



**Fig. 2.** a. TEM and b. – d. HRTEM images of P-600. g. & h. EELS C-k and B-k edge maps of local area shown in e. & f. in P-600. The EELS carbon k-edge fingerprint spectrum for glassy carbon and  $B_4C$  are compared in i.

TEM to explain the strengthening mechanism found in the P-600 samples.

Fig. 2a clearly shows two  $HfB_2$  particles connected by a nanosheet stack. Although these sheets exhibit a layered structure, no clear lattice

fringes could be observed from their basal plane, Fig. 2b. In an enlarged view of the junction between the nanosheets and  $HfB_2$  grains, Fig. 2c, some particles <5 nm in size but with good crystallinity were found. Some of the interplanar spacings of these particles are shown in

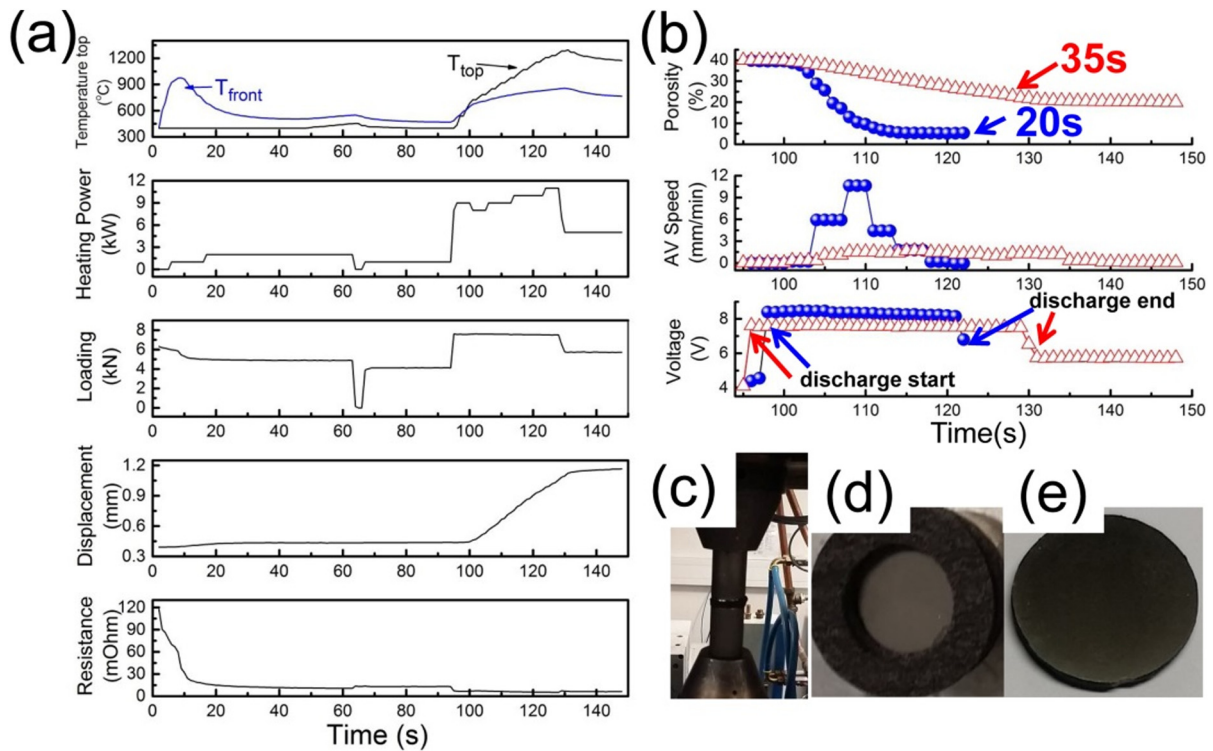


**Fig. 3.** SPS output curves recorded during FSPS of P-600. a. The set relative power is 80% with a discharging time of 35 s, b. the densification behaviour comparison of two samples with different FSPS parameters, discharging time 35 s, relative power 80% and discharging time 20 s, relative power 100%. (c) The digital images of the set-up for FSPS in a conventional SPS furnace, (d) P-600 before and (e) after FSPS.



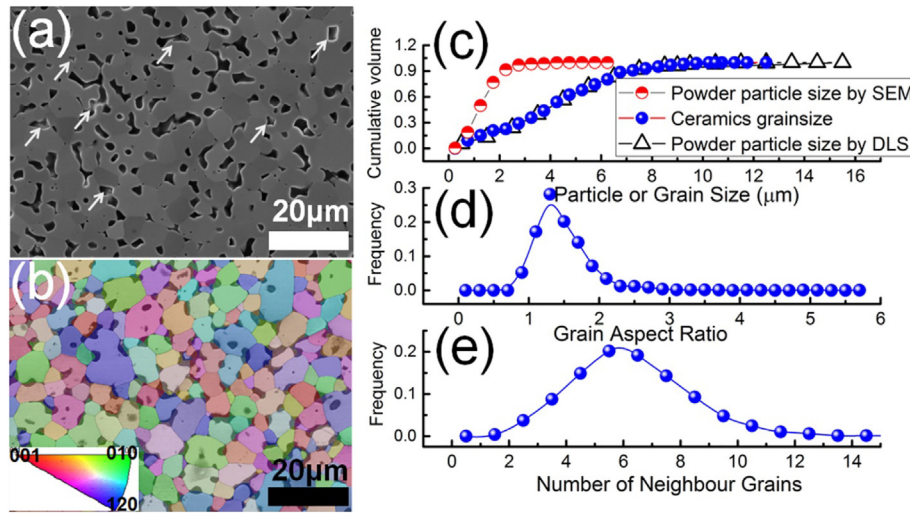


**Fig. 4.** a. The polished surface of a flash-SPSed P-600 sample produced using a discharge time of 20 s and 100% of the relative power. The orientation map from EBSD is shown in b. (Note that a. & b. were collected from slightly different areas of the same sample since the FIB used did not have a BSE detector and the image was tilted to 70°; it is extremely difficult to find the same area for EBSD using a different SEM). c. – e. show the distribution of the HfB<sub>2</sub> initial powder particle size determined by dynamic light scattering (DLS) and SEM, and the subsequent ceramic grain size, aspect ratio and number of neighbouring grains calculated based on the EBSD measurements respectively.

Fig. 2c; some fit with B<sub>4</sub>C (4.50, 3.78 and 2.37 Å), whilst the others (3.36 and 3.37 Å) are similar to the (0002) spacing of graphite (3.38 Å). The nanosheets not only bridge the adjacent particles, arrowed in Fig. 2a and 2e, they also coat the surface of some of the HfB<sub>2</sub> grains, as revealed by the HRTEM image in Fig. 2d.

According to the EELS maps of carbon and boron, Fig. 2g & h, a layer only containing carbon, region I in Fig. 2h, was observed to cover the edge of an HfB<sub>2</sub> particle, arrowed in Fig. 2f. Between the carbon layer and the HfB<sub>2</sub> particle, region III in Fig. 2h, an ~50 nm transition zone was observed composed of B and C, region II in Fig. 2h. The bonding between the carbon and HfB<sub>2</sub> appears to be quite strong since the carbon coating seems to be chemically anchored.

Ionisation edges corresponding to C-k were also found in the EELS patterns of the nanosheets, which show two peaks centred at about 287 and 298 eV, respectively, Fig. 2i. The first sharp peak belongs to the transitions of the  $\pi^*$  molecular orbital due to the existence of sp<sup>2</sup> bonded carbon, whilst the second more intense peak at 298 eV was induced by the  $\sigma^*$  orbitals transitions of carbon [17]. The slight broadening of the latter peak is a characteristic for glassy carbon; in amorphous carbon it is normally significantly broader compared to glassy carbon [17]. Glassy carbon is a non-graphitic carbon mainly constituted of sp<sup>2</sup> bonded atoms. It can exist as clusters or ribbons of graphite-like sheets interspersed with regions of amorphous carbon [18]. Both the EELS and HRTEM observations in Fig. 2 suggest that the PyC flakes derived from the PR are likely to be glassy carbon, which has a relatively high modulus of ~30 GPa and flexural strength of ~190 MPa [19]. If correct, both the bridging and coating of glassy carbon nanosheets on the HfB<sub>2</sub> particles will have been responsible for the higher strength in the P-600 compared to the P-RT.

The change in the sintering parameters during FSPS, including electrical resistance, displacement, electric current, SPS heating power and resulting front pyrometer temperature, are shown in Fig. 3. When a

sample with an electrical resistance of R is subjected to a voltage of V, the sample heating rate (dT/dt) may be expressed as Eq.1 [5].

$$\frac{dT}{dt} = \frac{1}{C} \left[ \frac{V^2}{R(T)} - \varepsilon\sigma(T^4 - T_f^4) \right] \quad (1)$$

where C and  $\varepsilon$  represent the sample's heat capacity and emissivity,  $\sigma$  is the Stefan–Boltzmann constant, T and T<sub>f</sub> are the temperature for the sample surface and furnace, respectively. It should be noted that Eq. (1) is not strictly applicable to current FSPS set-up as it neglects the Joule heating of the carbon felt and its low thermal conductivity. Unlike most oxides [2, 6], the electrical resistance of metal diborides such as HfB<sub>2</sub> increases linearly with temperature [20]. Therefore, dT/dt will decrease when a constant voltage is applied to HfB<sub>2</sub>-based samples and flash heating (an exponential increase in heating rate) will not occur without an additional sharp increase in the voltage.

As has been discussed previously [11], at the beginning of FSPS the current preferentially passed through the carbon felt, as shown by the initial temperature increase recorded by the front pyrometer (T<sub>f</sub>), Fig. 3a. This effectively caused the samples to be preheated. Subsequently, the current began to flow through the sample, leading to a drop in T<sub>f</sub> and a simultaneous decrease in electrical resistivity for the circuit, Fig. 3a. When the discharge began, a simultaneous increase in displacement and the top temperature, T<sub>t</sub>, was observed, Fig. 3a. The densification behaviour of HfB<sub>2</sub> ceramics during FSPS was strongly depending on the flash; Fig. 3b shows that a shorter discharge time and higher relative power was helpful in causing a more obvious flash and, consequently, an enhanced shrinkage rate. The porosity of the HfB<sub>2</sub> decreased to <5 vol% when discharge occurred in 20 s, whilst when it took 35 s the porosity did not decrease below 20 vol%, Fig. 3b.

**Table 1**

Preliminary calculations for the energy consumption used when densifying HfB<sub>2</sub>-based ceramics using conventional SPS, FSPS and modified FSPS in this work.

	Conventional SPS	Flash SPS (FSPS)	Modified flash SPS in this work
Sintering conditions	Heating from RT to 2100 °C over 20 min followed by a hold at 2100 °C for 30 min	Holding at 1600 °C for 20 min by SPS plus FSPS at 20 kW for 20 s	Holding at 600 °C for 2 h plus FSPS at 20 kW for 20 s
Approx. energy consumption per 100 pellets with the same size as used in this work/kWh	$7 \times 100 = 700$	$(2 + 0.2) \times 100 = 220$	$(2 \times 10/100 + 0.2) \times 100 = 40$

Most of the  $\text{HfB}_2$  samples sintered using FSPS were crack-free in this work, Fig. 3e. A mean relative density of 95.1% was obtained for the ceramics densified using a discharge time of 20 s and a relative power of 100%. Residual pores can be clearly seen, they are visible as dark regions with slightly bright edges from charging and are highlighted in some cases by arrows in Fig. 4a. Other areas with a dark contrast indicate  $\text{B}_4\text{C}$  and carbon grains. Both pores and  $\text{B}_4\text{C}$  grains are mainly located at the grain boundaries, as shown in the grain orientation map, Fig. 4b. The latter also confirms that no texturing was generated during densification. The average  $\text{HfB}_2$  grain size in the sintered bodies was  $\sim 4 \mu\text{m}$ , Fig. 4c, slightly larger than that of the reported average particle size of  $3.7 \mu\text{m}$ . This value is much larger than the primary particle size of  $\text{HfB}_2$  in the green body determined by SEM,  $\sim 1.25 \mu\text{m}$ , indicating densification and grain growth still compete with each other during FSPS as in conventional sintering. The final microstructure had equiaxed morphology with an average aspect ratio of  $\sim 1.2$  for the  $\text{HfB}_2$  grains, Fig. 4d. The number of neighbouring grains calculated, Fig. 4e, fits a normal distribution and the average value is close to six. Although the  $\text{HfB}_2$  ceramics were rapidly densified in only 20 s during FSPS, the resultant microstructures still resembled those sintered more conventionally. Based on the calculations in Table 1, by utilizing a proper design and optimization process for the green forming, the energy cost of FSPS could be further reduced by up to 80%, compared to FSPS using normal pre-heating.

In summary, starting with coarse  $\text{HfB}_2$  powder,  $>95\%$  dense  $\text{HfB}_2$  ceramics were achieved by FSPS in a discharge time of just 20 s, using 2 wt%  $\text{B}_4\text{C}$  and 1 wt% C as sintering aids. This work also demonstrates that pre-sintering, which is routinely adopted for flash SPS, is not necessary if ceramic green bodies strengthened by the presence of 1 wt% of glassy carbon are used.

## Acknowledgements

The work was supported by grants from the UK's Engineering and Physical Science Research Council entitled 'Materials Systems for

Extreme Environments', grant number EP/K008749/2 and 'Multiscale tuning of interfaces and surfaces for energy applications', grant number EP/P007821/1.

## References

- [1] M. Cologna, B. Rashkova, R. Raj, J. Am. Ceram. Soc. 93 (2010) 3556.
- [2] J. Luo, Scr. Mater. 146 (2018) 260.
- [3] R.I. Todd, E. Zapata-Solvas, R.S. Bonilla, T. Sneddon, P.R. Wilshaw, J. Eur. Ceram. Soc. 35 (2015) 1865.
- [4] W. Ji, B. Parker, S. Falco, J.Y. Zhang, Z.Y. Fu, R.I. Todd, J. Eur. Ceram. Soc. 37 (2017) 2547.
- [5] Y.H. Dong, I.W. Chen, J. Am. Ceram. Soc. 98 (2015) 3624.
- [6] Y. Zhang, J. Jung, J. Luo, Acta Mater. 94 (2015) 87.
- [7] S. Grasso, Y. Sakka, N. Rendtorff, C. Hu, G. Maizza, H. Borodianska, O. Vasylykiv, J. Ceram. Soc. Jpn. 119 (2011) 144.
- [8] R. Raj, M. Cologna, J.S.C. Francis, J. Am. Ceram. Soc. 94 (2011) 1941.
- [9] S. Grasso, T. Saunders, H. Porwal, O. Cedillos-Barraza, D.D. Jayaseelan, W.E. Lee, M.J. Reece, J. Am. Ceram. Soc. 97 (2014) 2405.
- [10] Y.H. Dong, I.W. Chen, J. Am. Ceram. Soc. 99 (2016) 2889.
- [11] S. Grasso, T. Saunders, H. Porwal, B. Milsom, A. Tudball, M. Reece, J. Am. Ceram. Soc. 99 (2016) 1534.
- [12] O. Vasylykiv, H. Borodianska, Y. Sakka, D. Demirskyi, Scr. Mater. 121 (2016) 32.
- [13] B. Niu, F. Zhang, J.Y. Zhang, W. Ji, W.M. Wang, Z.Y. Fu, Scr. Mater. 116 (2016) 127.
- [14] H.J. Brown-Shaklee, W.G. Fahrenholtz, G.E. Hilmas, J. Am. Ceram. Soc. 94 (2011) 49.
- [15] J. Zou, G.J. Zhang, Y.-M. Kan, T. Ohji, Scr. Mater. 62 (2010) 159.
- [16] J. Zou, G.J. Zhang, Y.-M. Kan, J. Eur. Ceram. Soc. 30 (2010) 2699.
- [17] K. Jurkiewicz, M. Pawlyta, D. Zygadlo, D. Chrobak, S. Duber, R. Wrzalik, A. Ratuszna, A. Burian, J. Mater. Sci. 53 (2018) 3509.
- [18] L.A. Pesin, J. Mater. Sci. 37 (2002) 1.
- [19] R.E. Bullock, J.L. Kaae, J. Mater. Sci. 14 (1979) 920.
- [20] L.N. Zhang, D.A. Pejaković, J. Marschall, M. Gasch, J. Am. Ceram. Soc. 94 (2011) 2562.